PHYSICAL REVIEW B **70**, 184432 (2004)

Critical sizes for ferromagnetic spherical hollow nanoparticles

D. Goll,[1,2] A. E. Berkowitz,[1] and H. N. Bertram[1]
[1]*Center for Magnetic Recording Research, University of California, San Diego, La Jolla, California 92093-0401, USA*
[2]*Max-Planck-Institut für Metallforschung, Heisenbergstrasse 3, D-70569 Stuttgart, Germany*

(Received 14 April 2004; revised manuscript received 27 August 2004; published 23 November 2004)

The total magnetic energies of zero-field magnetization states of ferromagnetic nanospheres with a nonmagnetic core are analytically calculated and compared with each other. The particle radius R_e and the thickness of the spheroidal shell R_e-R_i $(0 \leq R_i \leq R_e$, R_i: hole/core radius) are systematically varied for different hard and soft magnetic materials. Based on the results, the corresponding phase diagrams of the lowest-energy configurations are derived. The phase diagrams identify two phases for materials of uniaxial anisotropy (Co: single domain, curling vortex; $Nd_2Fe_{14}B$, FePt: single domain, two domain) and materials of cubic anisotropy (permalloy, Fe: single domain, curling vortex). In the case of hard magnetic materials the critical diameter for which the single-domain state becomes energetically unfavorable can become more than doubled for ultrathin spheroidal shells $(\varepsilon = R_i/R_e > 0.85)$ compared to the corresponding bulk sphere of the same particle size. As the stray field in a single-domain spherical hollow nanoparticle is inhomogeneous, the nucleation process takes place inhomogeneously starting at the magnetic poles of the inner surface at R_i.

DOI: 10.1103/PhysRevB.70.184432 PACS number(s): 75.50.Tt, 75.60.Ch, 75.50.Ww, 75.50.Bb

I. INTRODUCTION

Single-domain nanoparticles which are stable with respect to thermal demagnetization are an important prerequisite for ultrahigh-density magnetic recording and integrated magnetoelectronic devices. Various physical and chemical methods have been employed to produce magnetic nanoparticles, including sputtering, metal evaporation, spark erosion, grinding, electrodeposition, solution phase metal salt reduction, and neutral organometallic precursor decomposition. Recently, the production of spherical hollow nanoparticles was achieved by applying two different methods. (1) Spark erosion method:[1–4] Spark erosion utilizing liquid nitrogen as the dielectric liquid results in spherical particles with a hollow inner spherical region. (2) Colloid chemistry method:[5] Thermal decomposition of dicobalt octacarbonyl $Co_2(CO)_8$ in combination with a transmetalation reaction with water free $AgClO_4$ results in bimetallic Ag/Co particles composed of a nonmagnetic Ag core and a ferromagnetic Co shell. The aim of this paper is to analyze the conditions under which hollow spheres can be single domain. In particular, we wish to determine how much larger a hollow sphere can be than a solid sphere while maintaining single domain behavior. This investigation can help clarify the question of how much the material's weight and cost could be reduced when applying hollow particles technologically, especially in the case of expensive materials.

A spherical hollow nanoparticle is illustrated in Fig. 1. Its geometry is fixed by the particle radius R_e and the thickness of the spheroidal shell R_e-R_i $(0 \leq R_i \leq R_e$, R_i: hole/core radius). Hollow ferromagnetic spheres have received only minimal theoretical attention due to a lack of experimental progress so far. Kronmüller[6] calculated the magnetization distribution in the environment of nonmagnetic cavities in infinitely extended ferromagnetic metals. He discovered that in the case of a homogeneous magnetization distribution the Lorentz field inside the hollow space is partly shielded since the magnetization tries to avoid magnetic surface charges. Shute *et al.*[7] gives a mathematical analysis of one-sided flux configurations: Spherical hollow structures have the surprising property that depending on the magnetic structure the Lorentz field in the hole may vanish and the outside dipolar field is dramatically reduced. By contrast, ferromagnetic spherical bulk particles have been a frequent object of investigation in the last decades. Due to the comparatively easy handling of the stray field for the bulk geometry, a number of problems could be solved by analytical micromagnetic calculations. The most significant considerations referred to the dependence of the total energy of the zero-field magnetization states on the particle diameter,[8–12] nucleation processes of single-domain particles (homogeneous rotation, curling mode, buckling mode),[15,16] approach to ferromagnetic saturation,[17] and switching times in the case of homogeneous rotation.[18–21]

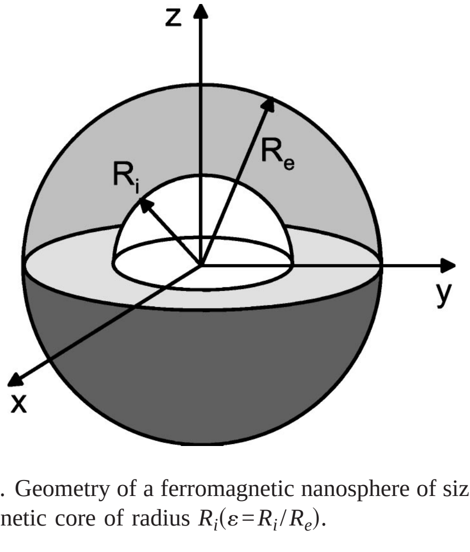

FIG. 1. Geometry of a ferromagnetic nanosphere of size R_e with a nonmagnetic core of radius $R_i(\varepsilon = R_i/R_e)$.

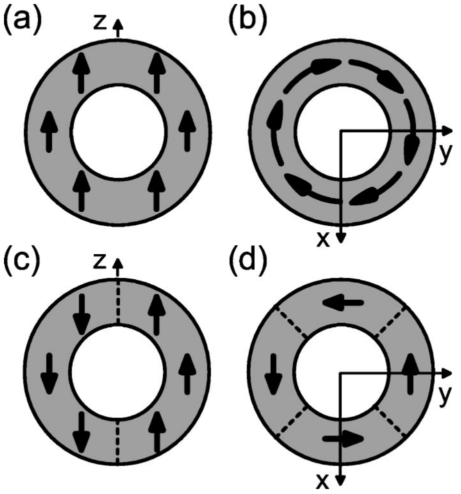

FIG. 2. Schematic representation of possible magnetization configurations in ferromagnetic nanospheres with a hollow core: (a) homogeneous or single-domain state, (b) curling-vortex state, (c) two-domain state, and (d) four-domain state.

A comparison of the total energies of zero-field magnetization states have resulted in single-domain configurations for small particles and internal flux closure arrangements, such as the curling-vortex state, two-domain state (only for uniaxial anisotropy), and four-domain state (only for cubic anisotropy) for larger particles.[8–10] In addition, for substantially larger particle sizes two cylindrically symmetric coaxial domains or multidomain configurations can be formed.[10–12] In general, these earlier comparisons neglected the energy of the vortices occurring in the curling-vortex state and the four-domain state.[9] Furthermore, the stray field energy of the two-domain state was assumed to be exactly one half of the single-domain state.[9] These results, achieved for the critical size below which the single-domain state is energetically favored, are only rough estimations. Analytical calculations of the vortex energy were only undertaken for cylindrical disks.[13,14] Here we perform complete energy comparisons for all the configurations shown in Fig. 2.

This paper is organized as follows. In Sec. II the formulas for calculating the total energies of the single-, two-, and four-domain states and of the curling-vortex state (including the energy of the vortex) are derived in dependence of the particle radius and the thickness of the spheroidal shell. In Sec. III we compare the energies of the different magnetization states with each other to find the lowest-energy configuration and the critical particle sizes denoting changes in the equilibrium state. The phase diagrams summerizing the prevailing magnetization states are set up for materials with uniaxial and cubic anisotropy, respectively. In Sec. IV the nucleation process of hollow nanospheres in the single-domain state is discussed and compared with the corresponding bulk spheres of the same material and particle size.

II. MAGNETIZATION STATES OF SPHERICAL HOLLOW PARTICLES

For bulk ferromagnetic nanospheres, in addition to the single-domain state, three other types of simple-domain structures tending towards flux closure may occur: the curling-vortex state (for low anisotropy), the two-domain state (for high anisotropy in a uniaxial crystal), and the four-domain state (for high anisotropy in a cubic crystal).[9] In the following we derive general expressions for the total energies of the four different magnetization states bearing in mind the variable nonmagnetic space of radius $0 \leqslant R_i \leqslant R_e$ in the interior of the nanospheres. Total energies in general are composed of magnetocrystalline energy, exchange energy, and stray field (magnetostatic) energy. The role of the surface anisotropy[22] will be discussed qualitatively at the end of Sec. III. The magnetoelastic energy plays no role in the following, since the particles are not embedded in a matrix. In Fig. 2 the four different magnetization configurations are schematically shown.

A. Single-domain state

The total energy of a hollow spherical particle in the homogeneous or single-domain state consists of stray field (magnetostatic) energy only. The stray field of the particle can be calculated by adding the stray fields resulting from the surface charges of the inner and outer spherical surfaces of radii R_i and R_e. The field due to the (uniform) magnetic charges on the inner surface (so-called Lorentz field), $H_L = J_s/(3\mu_0)$ ($J_s = \mu_0 M_s$: spontaneous polarization), and the inverse Lorentz field due to the outer surface $H_i = -J_s/(3\mu_0)$ compensate each other. Accordingly, the total field inside the hole vanishes:

$$H_z^{\text{hole}} = H_L + H_i = 0. \tag{1}$$

The stray field within the spheroidal shell at the point R ($R_i \leqslant R \leqslant R_e$)) is

$$H_z^{\text{shell}} = -\frac{J_s}{3\mu_0} - \frac{J_s}{3\mu_0}\left(\frac{R_i}{R}\right)^3 (3\cos^2\theta - 1). \tag{2}$$

The first term describes the inverse Lorentz field of the magnetic charges of the outer surface and the second term is the dipole field resulting from the surface charges of the inner surface. The stray field energy of the single-domain state is then obtained by integrating over the particle volume V

$$\phi_{\text{tot}}^{\text{hom}} = -\frac{1}{2}\int H_z^{\text{shell}} J_z dV = \frac{2}{9}\pi\frac{1}{\mu_0} J_s^2 R_e^3 (1-\varepsilon^3), \tag{3}$$

where $\varepsilon = R_i/R_e$ is the ratio of the two characteristic radii of the hollow particle.

It should be noted that in a more refined consideration, the shielding effect[6] due to inclined magnetization must be included. This inclination results from the inhomogeneous dipolar fields at the surface of the hole; the magnetization distribution becomes slightly inhomogeneous reducing the surface charges at R_i. This effect is not taken into account in

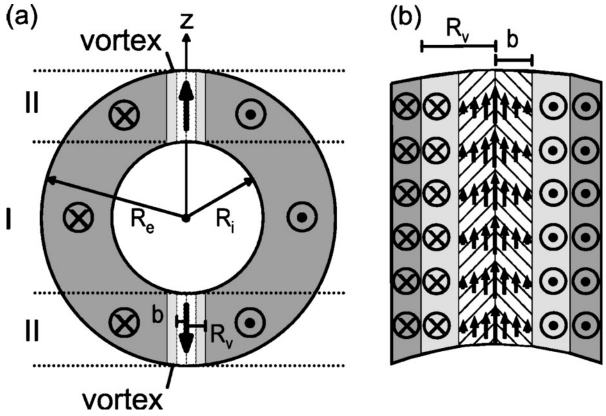

FIG. 3. Schematic representation of the curling-vortex state in detail: (a) The hollow nanosphere is subdivided into three regions [I: main body ($-R_i \leqslant z \leqslant R_i$), II: spherical caps, III: vortex region (R_v: radius of the vortex region, b: radius of the vortex core)]. (b) Vortex region enlarged to illustrate the curling magnetization distribution.

the following because it leads to a reduction of the Lorentz field by only a few percent.[6]

B. Curling-vortex state

For calculating the total energy of the curling-vortex state the hollow spherical particle is subdivided into three regions as illustrated in Fig. 3(a). Here, we take into account the formation of two vortices which avoids the singularity of the exchange energy. Assuming that curling occurs in the (x,y) plane, region I denotes curling around the hole $(-R_i < z < R_i)$, region II describes curling in the two caps of the sphere without the vortex regions (III or index v). Approximately, both vortex regions can be considered as cylindrical disks of radius R_v and height $R_e(1-\varepsilon)$. The vortex regions have a core of radius b inside which the magnetization has a nonzero component perpendicular to the plane of the disk; in the outer regions of the vortices (between b and R_v) the magnetization vector lies completely in the plane. The magnetization configuration is independent of the z coordinate along the disk axis [see Fig. 3(b)]. The energy of the curling-vortex state becomes minimal, when the orientation of the two vortices are oriented antiparallel to each other (see Fig. 3). However, the influence of the interaction between the two vortices is neglected; the approximation is justified in the following because the long-range stray fields of the vortices correspond to those of a quadrupole decreasing as $1/r^4$. The total energy is the sum of exchange, magnetocrystalline anisotropy energy and the vortex energies given by

$$\phi_{\mathrm{tot}}^{\mathrm{curling}} = \phi_A^{\mathrm{I}} + \phi_K^{\mathrm{I}} + 2\phi_A^{\mathrm{II}} + 2\phi_K^{\mathrm{II}} + 2\phi_A^{v} + 2\phi_K^{v} + 2\phi_S^{v}. \quad (4)$$

Whereas in regions I and II only exchange energy ϕ_A and magnetocrystalline anisotropy energy ϕ_K occur, in the vortex regions (index v) the stray field energy ϕ_S additionally must be included. For clarity we give the energy expressions separately.

1. Exchange energy of regions I and II

The exchange energy in region I is given by

$$\phi_A^{\mathrm{I}} = A\int (\nabla\varphi)^2 dV = A\int \frac{1}{x^2+y^2}dV$$

$$= A\int_{-R_i}^{R_i}\int_0^{2\pi}\int_{\sqrt{R_i^2-z^2}}^{\sqrt{R_e^2-z^2}} \frac{1}{\rho}\,d\rho\, d\varphi\, dz = 2\pi A\int_{-R_i}^{R_i} \ln\frac{\sqrt{R_e^2-z^2}}{\sqrt{R_i^2-z^2}}dz$$

$$= 2\pi A\left\{\int_0^{R_i} \ln(R_e^2-z^2)dz - \int_0^{R_i} \ln(R_i^2-z^2)dz\right\}$$

$$= 2\pi A\left(R_e \ln\frac{R_e+R_i}{R_e-R_i} + R_i \ln\frac{R_e^2-R_i^2}{4R_i^2}\right), \quad (5)$$

where $\varphi = -\arctan(y/x)$ is the polar angle of the magnetization vector and $\rho = \sqrt{x^2+y^2}$. The exchange energy of the two spherical caps (region II) is calculated as

$$2\phi_A^{\mathrm{II}} = 4\pi A\int_{R_i}^{R_e} \ln\frac{\sqrt{R_e^2-z^2}}{R_v}dz = 2\pi A\left(2R_e \ln\frac{2R_e}{R_v} + R_e \ln\frac{R_e-R_i}{R_e+R_i} - R_i \ln\frac{R_e^2-R_i^2}{R_v^2}\right). \quad (6)$$

2. Magnetocrystalline energy of regions I and II

The magnetocrystalline anisotropy energy of regions I and II of volume $V^{\mathrm{I+II}} = (4\pi/3)R_e^3(1-\varepsilon^3) - 2\pi R_v^2 R_e(1-\varepsilon)$ in the case of uniaxial anisotropy and anisotropy axis in the (x,y) plane is

$$\phi_K^{\mathrm{I}} + 2\phi_K^{\mathrm{II}} = \frac{1}{2\pi}V^{\mathrm{I+II}}\int_0^{2\pi} K_1 \sin^2\varphi\, d\varphi = \frac{1}{2}K_1 V^{\mathrm{I+II}}. \quad (7)$$

In the case of uniaxial anisotropy and anisotropy axis along the z axis we obtain

$$\phi_K^{\mathrm{I}} + 2\phi_K^{\mathrm{II}} = K_1 V^{\mathrm{I+II}} \quad (8)$$

and in the case of cubic anisotropy

$$\phi_K^{\mathrm{I}} + 2\phi_K^{\mathrm{II}} = \frac{1}{2\pi}V^{\mathrm{I+II}}\int_0^{2\pi} K_1(\gamma_1^2\gamma_2^2 + \gamma_1^2\gamma_3^2 + \gamma_2^2\gamma_3^2)d\varphi = \frac{1}{8}K_1 V^{\mathrm{I+II}} \quad (9)$$

with the direction cosines $\gamma_1 = \sin\varphi$, $\gamma_2 = \cos\varphi$, $\gamma_3 = 0$.

3. Vortex energy—region III

For deriving the exchange, anisotropy and stray field energies of the vortex regions we take the analytical calculations of Usov *et al.*[13] performed on cylindrical disks in the vortex state as a basis. The magnetization distribution inside the core of the vortex ($\rho \leqslant b$) is described by the direction cosines (polar coordinates ρ and φ)

$$\gamma_1 = -\frac{2\rho b}{\rho^2+b^2}\sin\varphi, \quad \gamma_2 = \frac{2\rho b}{\rho^2+b^2}\cos\varphi,$$

$$\gamma_3 = -\sqrt{1-\frac{4b^2\rho^2}{(\rho^2+b^2)^2}}. \tag{10}$$

The magnetization distribution outside the core ($b \leqslant \rho \leqslant R_v$) is given by

$$\gamma_1 = -\sin\varphi, \quad \gamma_2 = \cos\varphi, \gamma_3 = 0. \tag{11}$$

With $V^v = 2\pi R_v^2 R_e(1-\varepsilon)$ as the volume of the two vortices and using the SI-unit system, the exchange energy of the vortex area is given by [Eq. (2) in Ref. 13]

$$2\phi_A^v = \frac{1}{2\mu_0} J_s^2 l_s^2 R_e(1-\varepsilon)\left(2 - \ln\frac{b}{R_v}\right), \tag{12}$$

where $l_s = (2\mu_0 A)^{0.5}/J_s$ is the exchange length of the material. The anisotropy energy of the vortex area in the case of uniaxial anisotropy and anisotropy axis in the (x,y) plane [Eq. (3b) in Ref. 13] is

$$2\phi_K^v = \frac{1}{2}K_1 V^v\left\{1 + (3 - 4\ln 2)\left(\frac{b}{R_v}\right)^2\right\} \tag{13}$$

and in the case of uniaxial anisotropy and anisotropy axis along the z axis [Eq. (3a) in Ref. 13]

$$2\phi_K^v = K_1 V^v\left\{1 - (3 - 4\ln 2)\left(\frac{b}{R_v}\right)^2\right\}. \tag{14}$$

Additionally, we have calculated the anisotropy energy for a cubic material:

$$2\phi_K^v = K_1\int\{\gamma_1^2\gamma_2^2 + \gamma_3^2(\gamma_1^2+\gamma_2^2)\}dV^v$$

$$= K_1 V^v\left\{\frac{1}{8} - \left(\frac{65}{24} - 4\ln 2\right)\left(\frac{b}{R_v}\right)^2\right\}. \tag{15}$$

The stray field energy of the vortex area can be written for the case $R_e(1-\varepsilon) \geqslant l_s$ as [Eqs. (5) and (8b) in Ref. 13]

$$\phi_s^v = \frac{2\pi J_s^2}{\mu_0} b^3\left\{0.083 - \left(\ln 2 - \frac{1}{2}\right)^2\frac{b}{R_e(1-\varepsilon)}\right\}. \tag{16}$$

The radius of the vortex core b is obtained according to Usov *et al.*[13] by minimizing the total energy of the vortex region. However, in the minimizing procedure we take into account the anisotropy energy, giving for the radius of the vortex core

$$b = \sqrt[3]{-\frac{q}{2} + \sqrt{D}} - \frac{1}{3}\frac{p}{\sqrt[3]{-q/2+\sqrt{D}}} + \frac{1}{3}\frac{c_2}{c_1}, \tag{17}$$

where

$$p = -\frac{1}{3}\frac{c_2^2}{c_1^2}, \tag{18}$$

$$q = -\frac{2}{27}\frac{c_2^3}{c_1^3} - \frac{l_s^2}{c_1}, \tag{19}$$

$$D = \frac{1}{27}\frac{c_2^3 l_s^2}{c_1^4} + \frac{1}{4}\frac{l_s^4}{c_1^2}, \tag{20}$$

$$c_1 = 12\pi \times 0.083\frac{1}{R_e(1-\varepsilon)}, \tag{21}$$

$$c_2 = \begin{cases} -\dfrac{4\pi\mu_0}{J_s^2}K_1(3 - 4\ln 2): & \text{uniaxial anisotropy [easy axis} \parallel (x,y)\text{ plane]}, \\ \dfrac{8\pi\mu_0}{J_s^2}K_1(3 - 4\ln 2): & \text{uniaxial anisotropy (easy axis} \parallel z\text{ axis)}, \\ \dfrac{8\pi\mu_0}{J_s^2}K_1\left(\dfrac{65}{24} - 4\ln 2\right): & \text{cubic anisotropy}. \end{cases} \tag{22}$$

In general, the configuration with uniaxial anisotropy in the (x,y) plane always leads to a lower total energy than for the configuration with the z axis as the easy axis. The volume of the curling regions is always larger than that of the vortex regions. The radius of the vortex core b is smaller than the exchange length l_s in nanoparticles. For a fixed particle size R_e, the vortex core radius decreases when the spheroidal shell is made thinner. In our calculation we define the radius of the vortex region R_v to be twice the value of the radius of the vortex core b ($R_v = 2b$). For very soft magnetic materials ($K_1 \to 0$), Eq. (17) simplifies to the solution of Usov *et al.*:[13]

$$b = 0.68 l_s\left(\frac{R_e(1-\varepsilon)}{l_s}\right)^{1/3}. \tag{23}$$

For very hard magnetic materials ($K_1 \geqslant 1$ MJ/m^3) the vortex core b reaches values significantly larger than the particle size R_e due to the large magnetocrystalline anisotropy energy. As a consequence, the curling-vortex state cannot occur in such materials.

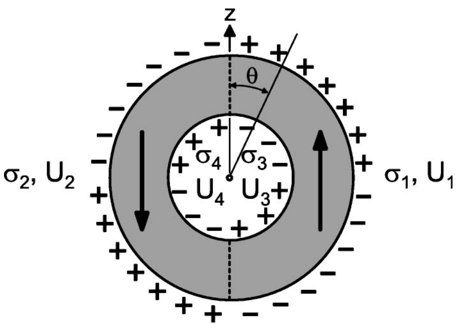

FIG. 4. Detailed schematic representation of the two-domain state of a ferromagnetic hollow nanoparticle as a shell octopole composed of two interacting quadrupoles of opposite sign.

C. Two-domain state

A hollow spherical particle in the two-domain state can be considered as a quasioctopole shell, which itself is composed of two interacting quadrupoles of opposite sign (see Fig. 4): The two surfaces each correspond to a quadrupole, however, with different surface charges. Thus the total energy is given by the sum of the stray field energy ϕ_s and the wall energy $\phi_{\rm wall}^{\rm two\ dom}$:

$$\phi_{\rm tot}^{\rm two\ dom} = \phi_s^{\rm outer\ quad} + \phi_s^{\rm inner\ quad} + \phi_s^{\rm interaction} + \phi_{\rm wall}^{\rm two\ dom}, \tag{24}$$

where $\phi_s^{\rm outer\ quad}$ and $\phi_s^{\rm inner\ quad}$ denote the stray field energies of the outer and inner quadrupole, respectively, and $\phi_s^{\rm interation}$ corresponds to the stray field energy resulting from the interaction between the two quadrupoles.

The stray field energy of the outer quadrupole is determined by surface charges $\sigma_j = \pm M_s \cos\theta\ (j=1,2)$ [where the $(+)$ sign holds for $0 \leqslant \varphi \leqslant \pi$ and the $(-)$ sign for $\pi \leqslant \varphi \leqslant 2\pi$] interacting with the potentials

$$U_i(r) = \frac{1}{4\pi}\int \frac{\sigma_i(r')}{|r-r'|} df' \tag{25}$$

resulting from surface charges $(i=1,2)$:

$$\begin{aligned}\phi_s^{\rm outer\ quad} &= \phi_{11} + \phi_{22} + \phi_{12} + \phi_{21}\\ &= \frac{1}{2}\mu_0 \sum_{i=1}^{2}\sum_{j=1}^{2}\int U_i(r)\sigma_j(r)df\\ &= \frac{\mu_0}{8\pi}\sum_{i,j}\int\int \frac{\sigma_i(r)\sigma_j(r')dfdf'}{|r-r'|}.\end{aligned} \tag{26}$$

From this, the four individual integrals are given by

$$\phi_{11} = \frac{J_s^2}{8\pi\mu_0}R_e^4 \int_0^{\pi}\int_0^{\pi} \cos\theta \sin\theta d\theta d\varphi \int_0^{\pi}\int_0^{\pi} \cos\theta' \sin\theta' \frac{1}{|r-r'|} d\theta' d\varphi', \tag{27}$$

$$\phi_{22} = \frac{J_s^2}{8\pi\mu_0}R_e^4 \int_{\pi}^{2\pi}\int_0^{\pi} \cos\theta \sin\theta d\theta d\varphi \int_{\pi}^{2\pi}\int_0^{\pi} \cos\theta' \sin\theta' \frac{1}{|r-r'|} d\theta' d\varphi',$$

$$\phi_{12} = \phi_{21} = -\frac{J_s^2}{8\pi\mu_0}R_e^4 \int_0^{\pi}\int_0^{\pi} \cos\theta \sin\theta d\theta d\varphi \int_{\pi}^{2\pi}\int_0^{\pi} \cos\theta' \sin\theta' \frac{1}{|r-r'|} d\theta' d\varphi' \tag{28}$$

with the surface element $df = R_e^2 \sin\theta d\theta d\varphi$. For the term $1/|r-r'|$ the following series expansion is used:[23]

$$\frac{1}{|r-r'|} = \sum_{n=0}^{\infty}\sum_{m=0}^{n} \varepsilon_m \frac{(n-m)!}{(n+m)!} P_n^m(\cos\theta) P_n^m(\cos\theta') \cos[m(\varphi - \varphi')] \begin{cases} \dfrac{r'^n}{r^{n+1}}, & r' < r,\\[2ex] \dfrac{r^n}{r'^{n+1}}, & r < r', \end{cases} \tag{29}$$

where the so-called Neumann factor ε_m is given by 1 for $m=0$ and by 2 for $m>0$. P_n^m are the associated Legendre functions containing the Legendre polynomials. In the case of the outer quadrupole $|r| = |r'| = R_e$.

As an example, we consider in the following the individual term ϕ_{11}, which may be representative for all four integrals. With the integral boundaries of Eq. (27) the following integrals are finite. For $m=0$ only $P_1(\cos\theta)$ gives a finite value given by

$$\phi_{11}^{m=0} = \frac{\pi}{18\mu_0} J_s^2 R_e^3. \tag{30}$$

The same amount results from $\phi_{22}^{m=0}$. However, ϕ_{12} and ϕ_{21} add just the negative values, thus compensating the ϕ_{ii} contributions. Accordingly, the total contribution due to $m=0$ is zero.

Contributions for $m>0$ are finite only for $m=2k+1$ (uneven m) and for $n=2l$ (even n) because the term $\cos m(\varphi-\varphi')=\cos m\varphi\cos m\varphi'+\sin m\varphi\sin m\varphi'$ gives finite integrals only for the $\sin m\varphi$ and $\sin m\varphi'$ terms, and these remain finite only for odd m. The integrals over φ and φ' give

$$\int_0^{\pi}\int_0^{\pi}\cos m(\varphi-\varphi')d\varphi d\varphi' = \frac{4}{m^2},$$

$$\int_0^{\pi}\int_{\pi}^{2\pi}\cos m(\varphi-\varphi')d\varphi d\varphi' = -\frac{4}{m^2}, \tag{31}$$

where always $m=2k+1$.

The finite terms of ϕ_{11} after the φ and φ' integration are

$$\phi_{11}^{m>0} = \frac{J_s^2}{\pi\mu_0}R_e^3\int_0^{\pi}\int_0^{\pi}\cos\theta\sin\theta\cos\theta'\sin\theta'\sum_{n=2l}^{\infty}\sum_{m=2k+1}^{2l-1}\frac{1}{m^2}\frac{(n-m)!}{(n+m)!}P_{2l}^{2k+1}(\cos\theta)P_{2l}^{2k+1}(\cos\theta')d\theta d\theta'. \tag{32}$$

Taking into account P_2^1, P_4^1, P_4^3, P_6^1, P_6^3, and P_6^5 results in

$$\phi_{11}^{m>0} = \frac{7741}{294912}\pi\frac{1}{\mu_0}J_s^2R_e^3. \tag{33}$$

In order to obtain the total stray field energy, the integral $\phi_{11}^{m>0}$ has to be multiplied by a factor 4 because ϕ_{22}, ϕ_{12}, and ϕ_{21} add the same value. This gives finally for the stray field of the outer quadrupole

$$\phi_s^{\text{outer quad}} = \frac{7741}{73728}\pi\frac{1}{\mu_0}J_s^2R_e^3 = \frac{1}{6\mu_0}J_s^2V_{\text{outer sphere}}\left(1-\frac{8643}{16384}\right)$$
$$= \frac{2}{9}\pi\frac{1}{\mu_0}J_s^2R_e^3(1-0.5275). \tag{34}$$

In other words, this result means that the bulk quadrupole reduces the stray field energy by approximately 47% as compared to the bulk dipole and shows that the estimate of Kittel[9] of a 50% reduction can be indeed used as a rough approximation.

The stray field energy of the inner quadrupole can be calculated in the same way resulting in

$$\phi_s^{\text{inner quad}} = \frac{7741}{73728}\pi\frac{1}{\mu_0}J_s^2R_i^3. \tag{35}$$

The stray field term $\phi_s^{\text{interation}}$ is determined by the eight interaction terms ϕ_{13}, ϕ_{31}, ϕ_{14}, ϕ_{41}, ϕ_{23}, ϕ_{32}, ϕ_{24}, and ϕ_{42}. All terms are negative and correspond each to $-\phi_{11}^{m>0}$, i.e., Eq. (32). However, the factors r'^n/r^{n+1} in Eq. (29) are now given by $2R_i/R_e$ in the case of P_2, by $2R_i^3/R_e^3$ in the case of P_4 and by $2R_i^5/R_e^5$ in the case of P_6 resulting in

$$\phi_s^{\text{interaction}} = -\frac{1}{16}\pi\frac{1}{\mu_0}J_s^2R_i^3\left(3\varepsilon+\frac{5}{18}\varepsilon^3+\frac{21}{256}\varepsilon^5\right). \tag{36}$$

The wall energy of the hollow spherical particle in the two-domain state is given by

$$\phi_{\text{wall}}^{\text{two dom}} = \pi\gamma^{180°}R_e^2(1-\varepsilon^2) \tag{37}$$

with the wall energy[24]

$$\gamma^{180°} = 2\pi\sqrt{\sqrt{2}-1}\sqrt{AK_1}+\frac{\pi J_s^2}{16\mu_0}R_e(1-\varepsilon). \tag{38}$$

For hard magnetic materials the second term in Eq. (38) can be neglected resulting in $\gamma^{180°}\cong 4\sqrt{AK_1}$. Inserting Eqs. (34)–(37) into Eq. (24) yields for the total energy

$$\phi_{\text{tot}}^{\text{two dom}} = \frac{1}{16}\pi\frac{1}{\mu_0}J_s^2R_e^3\left\{\frac{7741}{4608}(1+\varepsilon^3)-\varepsilon^3\left(3\varepsilon+\frac{5}{18}\varepsilon^3\right.\right.$$
$$\left.\left.+\frac{21}{256}\varepsilon^5\right)\right\}+\pi\gamma^{180°}R_e^2(1-\varepsilon^2). \tag{39}$$

The two-domain state only develops when the (uniaxial) anisotropy is large enough and/or the particle size is appreciably larger than the thickness δ of the 180° domain wall in the material[9,24]

$$\delta = \sqrt{\frac{4A}{K_1}(\sqrt{2}-1)}\left(1-\frac{1}{64(\sqrt{2}-1)}\frac{J_s^2R_e^2(1-\varepsilon)}{\mu_0A}\right). \tag{40}$$

In this case the anisotropy and exchange energies are equal in the domain wall. Otherwise, if the alteration in the spin direction is forced to take place in a distance less than the wall thickness, the exchange energy will be dominant. In the latter case the curling-vortex configuration is energetically preferred.

D. Four-domain state

A hollow spherical particle in the four-domain state as shown in Fig. 2(d) corresponds to a sixteen-pole shell composed of two interacting octopoles of opposite sign with the same vortex regions in the spherical caps, as we have already treated for the curling-vortex state. In this case the total energy is given by

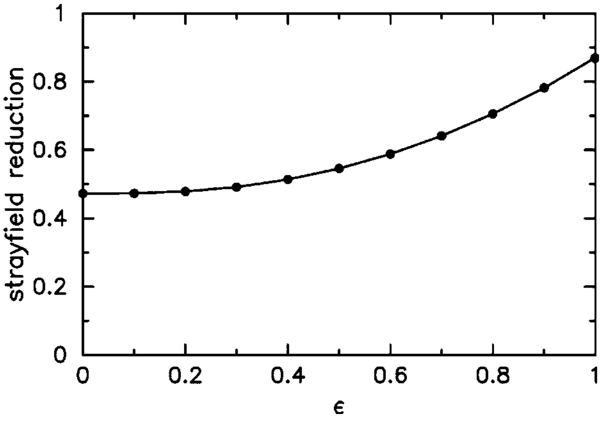

FIG. 5. Ratio $(\phi_{\text{tot}}^{\text{two dom}}-\phi_{\text{wall}}^{\text{two dom}})/\phi_{\text{tot}}^{\text{hom}}$ of the stray field energy of the two-domain state [Eqs. (24), (37), and (39)] to the stray field energy of the single-domain state [Eq. (3)] as a function of $\varepsilon = R_i/R_e$.

$$\phi_{\text{tot}}^{\text{four dom}} = \phi_s^{\text{four dom}} + \phi_{\text{wall}}^{\text{four dom}} + 2\phi_A^v + 2\phi_K^v + 2\phi_s^v. \tag{41}$$

The calculation of the stray field energy of a sixteen pole $\phi_s^{\text{four dom}}$, is much more complex than of an octopole. Therefore we only estimate this energy in the following. In Fig. 5 the reduction of the stray field energy dependence on the parameter ε due to the transformation of the single-domain state into the two-domain state is determined. The stray field reduction is maximal for the bulk particle, and decreases continuously with increasing volume of the nonmagnetic core from 47% ($\varepsilon=0$) to 87% ($\varepsilon=1$). We assume, that the same reduction occurs once more when the two-domain state (octopole state) is transformed into the four-domain state (sixteen-pole state). Therefore, we can write approximately for the stray field energy

$$\phi_s^{\text{four dom}} = \frac{(\phi_{\text{tot}}^{\text{two dom}} - \phi_{\text{wall}}^{\text{two dom}})^2}{\phi_{\text{tot}}^{\text{hom}}}, \tag{42}$$

where the stray field energies of the single-domain state $\phi_{\text{tot}}^{\text{hom}}$ and of the two-domain state $(\phi_{\text{tot}}^{\text{two dom}}-\phi_{\text{wall}}^{\text{two dom}})$ are given in Eq. (3) and eqs. (24), (37), and (39), respectively.

The wall energy of the hollow spherical particle in the four-domain state $\phi_{\text{wall}}^{\text{four dom}}$ is, when the vortex regions are excluded,

$$\phi_{\text{wall}}^{\text{four dom}} = \{2\pi R_e^2(1-\varepsilon^2) - 8R_vR_e(1-\varepsilon)\}\gamma^{90°} \tag{43}$$

with the wall energy $\gamma^{90°}=0.32\gamma^{180°}$[24] and $\gamma^{180°}$ defined in Eq. (37). The energy of the vortex regions and the extention of the vortex core are the same as calculated for the curling-vortex state [see Eqs. (10)–(23)]. Similarly to the two-domain state, the calculation of the four-domain state is only applicable if the cubic anisotropy is large enough and/or the particle size R_e is larger than the wall thickness.

III. CRITICAL PARTICLE SIZES

After deriving the total energies of the different magnetization states we now compare the energies with each other for different material parameters to find the lowest-energy configuration. We focus on the particle size R_e and the relative core diameter $\varepsilon=R_i/R_e$ (Fig. 1), as well as on the critical particle sizes R_e^{crit} at which one magnetization state transforms into another one as the total energies of two configurations become equal.

A. Determination of the critical particle sizes

A simple explicit expression for the critical size R_e^{crit} can be found for hard magnetic materials by comparing the total energy of the single-domain state [Eq. (3)] with the total energy of the two-domain state [Eq. (39)]:

$$R_e^{\text{crit}} = \frac{32\mu_0\gamma^{180°}}{J_s^2}\,\frac{1-\varepsilon^2}{\dfrac{2881}{768} - \dfrac{24125}{2304}\varepsilon^3 + 6\varepsilon^4 + \dfrac{5}{9}\varepsilon^6 + \dfrac{21}{128}\varepsilon^8}, \tag{44}$$

where $\gamma^{180°}=4\sqrt{AK_1}$. For the limiting case $\varepsilon=0$ (bulk particle) Eq. (44) reaches the values

$$R_e^{\text{crit}}(\varepsilon=0) = \frac{32\mu_0\gamma^{180°}}{J_s^2}\frac{768}{2881}. \tag{45}$$

This result corresponds approximately to the estimation $9\mu_0\gamma/J_s^2$ published by Kittel.[9] For the limiting case $\varepsilon=1$ (infinitely thin spheroidal shell), Eq. (44) results in

$$R_e^{\text{crit}}(\varepsilon=1) = \frac{32\mu_0\gamma^{180°}}{J_s^2}\frac{1536}{2125}. \tag{46}$$

Comparing the two limiting cases

$$\frac{R_e^{\text{crit}}(\varepsilon=1)}{R_e^{\text{crit}}(\varepsilon=0)} = \frac{5762}{2125} \cong 2.71 \tag{47}$$

leads to the conclusion that the critical radius for the phase transition from the single-domain to the two-domain state is significantly shifted to higher values.

For all the other phase transitions in principle possible in ferromagnetic hollow nanoparticles between two different magnetization patterns, no explicit solutions for R_e^{crit} exist. However, the solutions for the various critical particle sizes can be determined graphically.

B. The exemplary case $\varepsilon=0.5$

In Fig. 6 the total energies of the different magnetization states are plotted versus the particle size R_e for ferromagnetic hollow particles with $\varepsilon=0.5$ made of FePt, Co, Fe, and permalloy, respectively. The material parameters used are summarized in Table I. In principle, in all cases the single-domain state is the energetically most favorable configuration for very small particle sizes and the total energies of the different magnetization patterns increase with increasing R_e. All phase transitions take place spontaneously as first order phase transitions.

For (uniaxial) FePt [Fig. 6(a)] only the single-domain state and the two-domain state have been taken into consideration, since the two-domain state is the only flux-closure

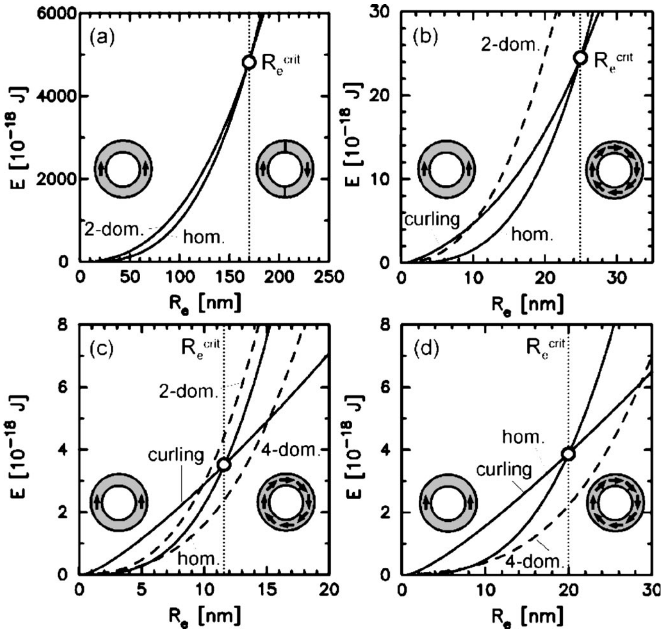

FIG. 6. Comparison of the total energies of the different magnetization states as a function of the particle size R_e for ferromagnetic hollow particles with $\varepsilon=0.5$: (a) FePt (uniaxial anisotropy), (b) Co (uniaxial anisotropy), (c) Fe (cubic anisotropy), and (d) permalloy (cubic anisotropy). The dashed curves correspond to those configurations which are not realized.

type arrangement with the major part of the magnetization oriented parallel to the uniaxial anisotropy axis, thereby reducing the magnetocrystalline anisotropy energy significantly. The curling-vortex state is not realized because of the large contribution of the magnetocrystalline anisotropy energy. With increasing particle size R_e the total energy of the single-domain state increases more rapidly than the total energy of the two-domain state. According to Eq. (44), at the critical particle size $R_e^{\text{crit}}=170$ nm, the total energies of the two magnetization configurations become equal and a phase transition between the single-domain state and the two-domain state takes place.

In contrast to hard magnetic materials in half-hard and soft magnetic materials the gain in magnetostatic energy exceeds the expansion of the magnetocrystalline energy, thus, leading to a vortex state at R_{crit}. For (uniaxial) Co [Fig. 6(b)], only the single-domain state and the curling-vortex state can occur as low-energy configurations, whereas the two-domain state (and of course the four-domain state) remains a high-energy configuration for all particle sizes R_e. At $R_e^{\text{crit}}=24.9$ nm the single-domain state transforms into the curling-vortex state whereby the vortex core b according to Eq. (17) is found to be 4.0 nm. At the critical diameter the total energy of the curling-vortex state is mainly determined by the exchange and anisotropy energies of the curling regions I and II, which are together a factor of 10 larger than the energy of the vortex regions.

TABLE I. Intrinisic material parameters used for FePt, Co, Fe, and permalloy (K_1: anisotropy constant, A: exchange constant, J_s: spontaneous polarization).

	FePt	Co	Fe	Permalloy
K_1 [J/m^3]	6.6×10^6	4.0×10^5	4.6×10^4	5.0×10^2
A [pJ/m]	10	30	20	10
J_s [T]	1.43	1.8	2.15	1.0
anisotropy	uniaxial	uniaxial	cubic	cubic

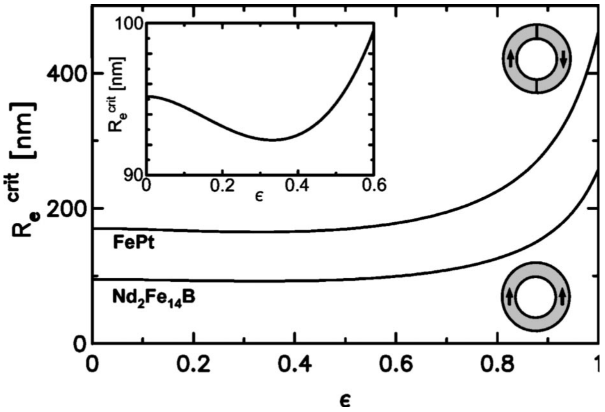

FIG. 7. Phase diagram of the lowest-energy magnetization configuration in FePt and $Nd_2Fe_{14}B$ hollow nanoparticles as a function of the parameter $\varepsilon=R_i/R_e$. The inset is a magnefication of R_e^{crit} for the $Nd_2Fe_{14}B$ curve from $\varepsilon=0$ to $\varepsilon=0.6$.

For (cubic) Fe and Permalloy [Figs. 6(c) and 6(d)] a similar behavior is obtained. Starting from small particle sizes and increasing R_e, the single-domain state transforms into the curling-vortex state at $R_e^{\text{crit}}=11.62$ nm in the case of Fe and at $R_e^{\text{crit}}=20.0$ nm in the case of permalloy. At the transition point the radius of the vortex core b amounts to 2.7 nm for Fe and is found to be 4.7 nm for permalloy. In both cases the total energy of the curling-vortex state is, at R_e^{crit}, principally determined by the exchange energy of the curling regions I and II, which is about a factor 10 larger than the energy of the vortex regions and about a factor 100 (Fe) or 1000 (Py) larger than the anisotropy energy of the curling regions. The phase transition between the single-domain state and the four-domain state, appearing at $R_e^{\text{crit}}=5.45$ nm (Fe) and at $R_e^{\text{crit}}=8.16$ nm (Py), cannot exist in reality, as these values are significantly smaller than the wall thicknesses given by Eq. (40) [$d(\text{Fe})=26.8$ nm, $d(\text{Py})=163.8$ nm]. The two-domain state does not occur as a low-energy configuration.

C. Phase diagrams

We generalize the results of Sec. III B above to a wide range of relative core diameters ($\varepsilon=R_i/R_e$) and plot phase diagrams that demark critical regions. In Fig. 7 the phase diagram of the lowest-energy magnetization configuration is shown for nanoparticles made of FePt and $Nd_2Fe_{14}B$. Below the phase boundary the single-domain state has the lowest total energy, above the phase boundary the two-domain state is energetically preferred. The critical particle size R_e^{crit} remains nearly constant for the ratio of inner radius to outer radius $\varepsilon\leqslant0.6$, i.e., the hollow sphere behaves the same as a bulk sphere but deviates by a factor of 1.055 according to

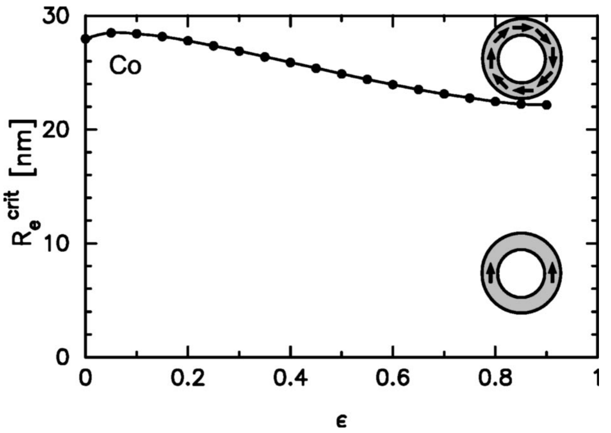

FIG. 8. Phase diagram of the lowest-energy magnetization configuration in Co hollow nanoparticles as a function of the parameter $\varepsilon = R_i/R_e$.

Eq. (45) from Kittel's estimation.[9] Further increase of the ε parameter leads to a large shift of the phase boundary to larger critical particle sizes according to Eq. (44) and results in a limiting value which is larger by a factor of 2.71 than the bulk value [see Eq. (47)]. This increase is due to the reduction of the magnetostatic energy when the thickness of the hollow spherical shell decreases. With decreasing thickness of the hollow spherical shell the magnetic charge distributions finally form an ideal octopole with a lower magnetostatic energy than the quadrupole configuration. The slight minimum of R_e^{crit} occurring for $\varepsilon = 0.33$ is a consequence of the complex dependence of R_e^{crit} on ε according to Eq. (44), but can be neglected in a first approximation. The phase diagram of Co nanoparticles is illustrated in Fig. 8. Here, the phase boundary separates single-domain state from the curling-vortex state (as the lowest-energy configuration) and not from the two-domain state. The phase boundary is shifted from $R_e^{\mathrm{crit}} = 28$ nm for $\varepsilon = 0$ to $R_e^{\mathrm{crit}} = 22.2$ nm for $\varepsilon = 0.9$. For small ε parameters a slight increase of R_e^{crit} is obtained up to 28.5 nm for $\varepsilon = 0.05$. A similar behavior is observed for Fe and permalloy, as seen in Fig. 9. However, the decrease of the critical particle size from the bulk particle to the $\varepsilon = 0.9$ shell particle is not as distinctive as in the case of Co. The bulk values of R_e^{crit} obtained for Fe and permalloy for the transformation of the single-domain state to the curling-vortex state are 12.16 and 20.88 nm, respectively. The R_e^{crit} values for $\varepsilon = 0.9$ are 10.67 and 18.4 nm, respectively.

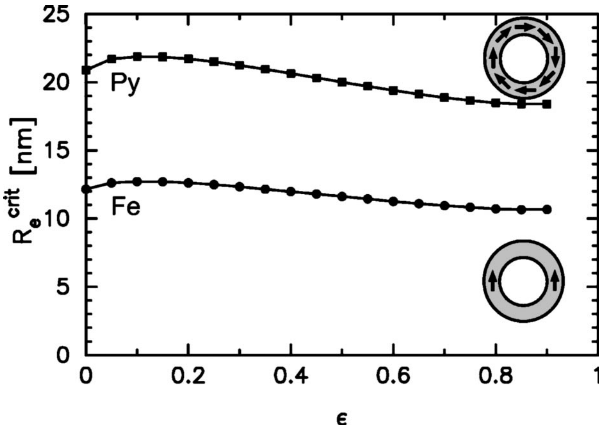

FIG. 9. Phase diagram of the lowest-energy magnetization configuration in Fe and permalloy hollow nanoparticles as a function of the parameter $\varepsilon = R_i/R_e$.

The phase diagrams have been determined by omitting surface anisotropy energies. In the case of the transition from the single-domain state to the two-domain state this approximation is correct as far as the depth of the surface area with finite surface anisotropy is smaller than the exchange length. In this case the surface anisotropy energy is the same for the single-domain and the two-domain state and therefore vanishes in the evaluation of R_e^{crit}. Effects of the surface anisotropy are expected for large ε parameters ($\varepsilon > 0.95$) and if the depth of the surface region becomes larger than the exchange length. In the case of the transition from the single-domain state to the curling-vortex state the surface anisotropy contributes to the total magnetocrystalline anisotropy energy by an amount which is proportional to the surfaces. In the evaluation of the critical radius this would lead to an increase of R_e^{crit}. This effect increases with increasing ε. For a quantitative analysis future calculations will be performed.

IV. NUCLEATION PROCESS FOR SINGLE-DOMAIN PARTICLES

For single-domain bulk nanoparticles the inner stray field $H_i = -J_s/(3\mu_0)$ is homogeneous. The stray field becomes inhomogeneously distributed when the single-domain particles are hollow. According to Eq. (2), the demagnetization field in the spheroidal shell is largest for $\theta = 0$ (and 180°) and at $R = R_i$ given by $H_z^{\mathrm{shell}} = -M_s$. Consequently, nucleation will start from these two poles initializing an inhomogeneous demagnetization process. For very small R_i (bulk limit), however, nucleation takes place by conventional homogeneous rotation.

V. CONCLUSIONS

We have derived phase diagrams of domain configurations for ferromagnetic hollow nanospheres as a function of the material parameters J_s, K_1, A, and the ratio ε of the internal and external radius of the hollow particles. With increasing particle size the phase diagrams separate a high-remanent single-domain phase of high magnetostatic energy from low-remanent domain states of low magnetostatic energy.

In hard magnetic materials (e.g., $Nd_2Fe_{14}B$, FePt) the phase transition takes place from the single-domain state to the low-remanent two-domain state. The critical particle size at which the phase transition occurs increases by a factor of 2.71 in ultrathin spheroidal shells as compared to the bulk value obtained for $\varepsilon < 0.6$.

In half-hard or soft magnetic materials (e.g., Co, Fe, permalloy) the phase transition takes place from the single-domain state to a low-remanent vortex state. This difference between the hard and soft magnetic materials results from the magnetocrystalline anisotropy energy which together with the magnetostatic energy is minimized in hard magnetic materials by the formation of the two-domain state. In soft magnetic materials the vortex state reduces the magnetostatic energy drastically and the magnetocrystalline energy remains always small.

In the case of FePt the single-domain state is stable up to a critical particle size of $R_e^{\mathrm{crit}}(\mathrm{FePt}) \approx 170$ nm for bulk particles $(\varepsilon < 0.6)$ and increases up to $R_e^{\mathrm{crit}}(\mathrm{FePt}) \approx 461$ nm for extremely thin hollow spherical shells. For Co and permalloy with increasing ε the critical radius decreases slightly from $R_e^{\mathrm{crit}}(\mathrm{Co}) = 28$ nm and $R_e^{\mathrm{crit}}(\mathrm{permalloy}) \approx 20.88$ nm for bulk particles to $R_e^{\mathrm{crit}}(\mathrm{Co}) \approx 22.2$ nm and $R_e^{\mathrm{crit}}(\mathrm{permalloy}) \approx 18.4$ nm for thin hollow spherical shells of $\varepsilon = 0.9$. Since the critical particle sizes for the single-domain state in all the cases are not substantially reduced, the use of hollow spherical particles instead of bulk particles in future applications can significantly reduce the material's weight and cost (in the case of expensive materials such as FePt).

In contrast to bulk spheres no homogeneous nucleation process exists in hollow spheres for the magnetization reversal of the single-domain state. Instead of this, the nucleation takes place inhomogeneously and starts at the internal poles of the single-domain particle where the demagnetizing field has its largest value of $(-)M_s$.

Further noteworthy results obtained in the present calculations are the following ones: In bulk spheres, the reduction of the magnetostatic energy due to the transition from the single-domain to the two-domain state is found to be given by a factor of $7739/16384 \approx 0.472$. This precise result confirms Kittel's previous assumption that the energy reduction corresponds to a factor of 0.500. The curling-vortex configuration has been investigated quantitatively including the vortices existing at the poles of the hollow particle. The energy of the two vortices was found to contribute only to 10% of the total energy which is mainly determined by exchange and magnetocrystalline anisotropy energies.

ACKNOWLEDGMENTS

The authors gratefully acknowledge fruitful discussions with H. Kronmüller and H. Radousky. This work was supported by the Postdoc-Programme of the German Academic Exchange Service (DAAD). A.E. Berkowitz was partially supported by a grant from the Lawrence Livermore National Laboratory under LDRD Contract No. B522317.

---

[1] A.E. Berkowitz and J.L. Walter, J. Mater. Res. **2**, 277 (1987).
[2] J. Carrey, H.B. Radousky, and A.E. Berkowitz, J. Appl. Phys. **95**, 823 (2004).
[3] V.C. Solomon, D.J. Smith, Y.J. Tang, and A.E. Berkowitz, J. Appl. Phys. **95**, 6954 (2004).
[4] A.E. Berkowitz, H. Harper, D.J. Smith, H. Hu, Q. Jiang, V.C. Solomon, and H.B. Radousky, Appl. Phys. Lett. **85**, 940 (2004).
[5] N.S. Sobal, M. Hilgendorff, H. Möhwald, M. Giersig, M. Spasova, T. Radetic, and M. Farle, Nano Lett. **2**, 621 (2002).
[6] H. Kronmüller, Z. Phys. **168**, 478 (1962).
[7] H.A. Shute, J.C. Mallinson, D.T. Wilton, and D.J. Mapps, IEEE Trans. Magn. **36**, 440 (2000).
[8] C. Kittel, Phys. Rev. **70**, 965 (1946).
[9] C. Kittel, Rev. Mod. Phys. **21**, 541 (1949).
[10] C.H. Stapper, J. Appl. Phys. **40**, 798 (1969).
[11] R. Carey and B.W.J. Thomas, J. Phys. D **8**, 342 (1975).
[12] I. Eisenstein and A. Aharoni, J. Appl. Phys. **47**, 321 (1976).
[13] N.A. Usov and S.E. Peschanyi, Phys. Met. Metallogr. **78**, 591 (1994).
[14] H. Hoffmann and F. Steinbauer, J. Appl. Phys. **92**, 5463 (2002).
[15] W.F. Brown, Phys. Rev. **105**, 1479 (1957).
[16] E.H. Frei, S. Shtrikman, and D. Treves, Phys. Rev. **106**, 446 (1957).
[17] H. Kronmüller, J. Appl. Phys. **52**, 1859 (1981).
[18] R. Kikuchi, J. Appl. Phys. **27**, 1352 (1956).
[19] T. Leineweber and H. Kronmüller, J. Magn. Magn. Mater. **192**, 575 (1999).
[20] J.C. Mallinson, IEEE Trans. Magn. **36**, 1976 (2000).
[21] K.Z. Gao, E.D. Boerner, and H.N. Bertram, J. Appl. Phys. **93**, 6549 (2003).
[22] M. Jamet, W. Wernsdorfer, C. Thirion, D. Mailly, V. Dupius, P. Melinon, and A. Perez, Phys. Rev. Lett. **86**, 4676 (2001).
[23] P.M. Morse and H. Feshbach, *Methods of Theoretical Physics* (McGraw Hill, New York, 1953), pt. II, p. 1274.
[24] D. Goll, G. Schütz, and H. Kronmüller, Phys. Rev. B **67**, 094414 (2003).